royalsocietypublishing.org/journal/rspa

Research

Cite this article: Downing CA, Weick G. 2020 Plasmonic modes in cylindrical nanoparticles and dimers. *Proc. R. Soc. A* **476**: 20200530. https://doi.org/10.1098/rspa.2020.0530

Received: 7 July 2020
Accepted: 16 November 2020

Subject Areas:
solid state physics, nanotechnology, optics

Keywords:
nanoplasmonics, nanoparticles, dimers, quantum-size effects

Author for correspondence:
Guillaume Weick
e-mail: guillaume.weick@ipcms.unistra.fr

THE ROYAL SOCIETY PUBLISHING

Plasmonic modes in cylindrical nanoparticles and dimers

Charles A. Downing[1,2] and Guillaume Weick[3]

[1]Departamento de Física de la Materia Condensada, CSIC-Universidad de Zaragoza, 50009 Zaragoza, Spain
[2]Department of Physics and Astronomy, University of Exeter, Exeter EX4 4QL, UK
[3]Université de Strasbourg, CNRS, Institut de Physique et Chimie des Matériaux de Strasbourg, UMR 7504, 67000 Strasbourg, France

CAD, 0000-0002-0058-9746; GW, 0000-0002-0617-5835

We present analytical expressions for the resonance frequencies of the plasmonic modes hosted in a cylindrical nanoparticle within the quasi-static approximation. Our theoretical model gives us access to both the longitudinally and transversally polarized dipolar modes for a metallic cylinder with an arbitrary aspect ratio, which allows us to capture the physics of both plasmonic nanodisks and nanowires. We also calculate quantum mechanical corrections to these resonance frequencies due to the spill-out effect, which is of relevance for cylinders with nanometric dimensions. We go on to consider the coupling of localized surface plasmons in a dimer of cylindrical nanoparticles, which leads to collective plasmonic excitations. We extend our theoretical formalism to construct an analytical model of the dimer, describing the evolution with the inter-nanoparticle separation of the resultant bright and dark collective modes. We comment on the renormalization of the coupled mode frequencies due to the spill-out effect, and discuss some methods of experimental detection.

1. Introduction

The optical properties of small metal clusters have been studied throughout the twentieth century [1], in a field which is now referred to as plasmonics [2]. Modern nanoplasmonics aims to confine and control light at the nanoscale, in an amalgamation of photonics and electronics [3]. It is envisaged that applications will arise in areas from data storage and microscopy to

light generation and biophotonics [4–6]. In the last few years, the subfield of quantum plasmonics has branched away, whereby quantum mechanical phenomena play a crucial role [7].

An intensively studied quasi-particle in plasmonics is the localized surface plasmon (LSP), a collective oscillation of conduction band electrons, which arises when a metallic nanoparticle (NP) is irradiated by light [2] or hot electrons [8]. Exploring how the resonance frequency of the plasmon changes depending on the geometry of its hosting NP is a fundamental task of the field [9–14]. Recently, a number of groundbreaking experiments [15–21] have probed the plasmonic response of metallic cylinders, and in particular the limiting cases of nanodisks and nanowires. Inspired by these experiments, in this work, we derive simple, analytical expressions for the dipolar plasmon resonances within the quasi-static limit (valid when the dimensions of the NP is smaller than the wavelength associated with the LSP resonance frequency) in both the longitudinal and transverse polarizations (that is, along the cylindrical axis and perpendicular to it). Our model is based upon a calculation of the change in Hartree energy of the NP due to the collective displacement of the valence electrons. We assume that the electrons in the nanostructure form a body of approximately uniform density, which allows us to employ continuum mechanics and set up a simple equation of motion [22]. Importantly, our analytic theory is valid for any aspect ratio of the cylinder, and as such is of relevance for a wide range of experiments. Our work therefore complements previous theoretical studies of plasmonic cylinders, which have either employed the nanowire approximation [23–25], or have required numerics [26–31].

In our model, the inevitable quantum corrections which arise at the nanoscale are addressed by accounting for the so-called spill-out effect [32]. In this quantum size effect, the resonance frequency is modified due to a proportion of electrons spilling outside of the small metallic NP, thus lowering the average electronic density inside the NP. This effect arises due to the ground-state many-body wave function, which determines the electronic density, having tails which leak outside of the sharp boundary of the NP surface, so that a non-negligible number of electrons reside outside of the cluster. The spill-out effect has been studied historically in relation to spherical NPs [22], and more recently has been investigated for plasmons in ultra-sharp groove arrays [33].

Coulomb interactions between LSPs housed in different NPs can give rise to collective plasmons spread out over the combined nanostructure [34,35]. The study of collective plasmons in NP arrays, including architectures built from cylindrical NPs [36–40], has led to a wealth of diverse physics, from plasmonic waveguides [41,42] to light harvesters [43,44] to analogues of a topological insulator [45–48]. In this work, we are concerned with the simplest example of a coupled system, the NP dimer [49–52], which constitutes the building block of more complex metastructures, and where insight into the nature of coupled plasmons can be achieved.

A series of experiments on nanoplasmonic dimers in the near-field coupling regime have revealed both bright and dark plasmonic modes, where the dipole moments are oriented in-phase or out-of-phase, respectively [53–55]. In order to account analytically for such collective plasmonic effects, we adapt our aforementioned theory to the case of a dimer of cylindrical metallic NPs. We derive simple expressions for the bright and dark mode resonance frequencies of the system as a function of the interparticle separation, which allows for a clear description of how the plasmonic coupling scales with distance. Our results supplement theories of cylindrical dimers in the literature, which predominately involve assumptions about the aspect ratio of the cylinder, or require time-consuming numerical computations [56–62]. We also comment on the spill-out effect in the dimer, and suggest some methods for the experimental detection of our predicted effects.

This paper is organized as follows. In §2, we calculate the dipolar resonances of a single cylindrical NP and discuss their respective decay rates. We find the modifications to the resonance frequencies due to the spill-out effect in §3. The theory is extended to describe collective effects in a dimer of cylindrical NPs in §4. Finally, we draw some conclusions in §5.

2. Plasmonic modes in a single cylindrical nanoparticle

We consider a cylindrical NP of radius a and length L, containing N_e valence electrons with charge $-e < 0$ and mass m_e (see the inset in figure 1). We start by neglecting the electronic spill-out

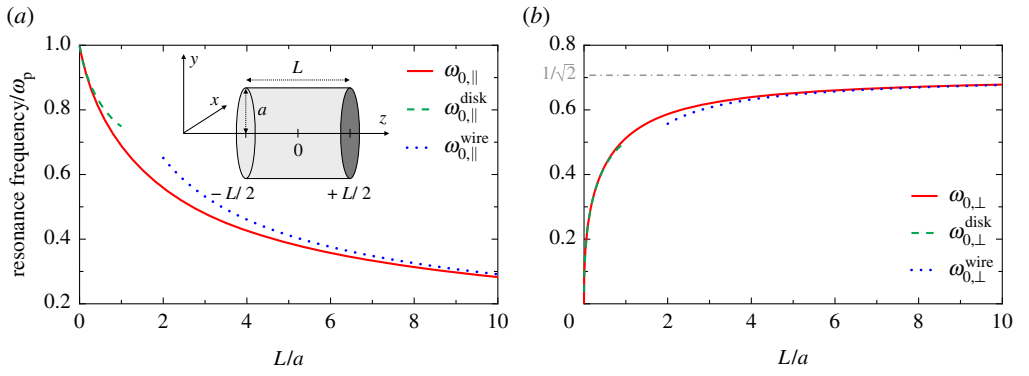

Figure 1. Resonance frequencies $\omega_{0,\parallel}$ and $\omega_{0,\perp}$ (solid red lines), in units of the plasma frequency ω_p, as a function of the aspect ratio L/a for both the (*a*) longitudinal (cf. (2.14)) and (*b*) transverse (cf. (2.20)) modes. Dashed green lines: the disk limit approximations, from (2.15) and (2.21) for panels (*a*) and (*b*), respectively. Dotted blue lines: the wire limit approximations, from (2.16) and (2.22) for (*a*) and (*b*), respectively. Horizontal dash-dotted line in (*b*): the asymptotic result $\omega_\mathrm{p}/\sqrt{2}$, for $L/a \to \infty$. Inset: sketch of a cylindrical metallic nanoparticle of radius a and length L. (Online version in colour.)

effect, and assume that the density $n(\mathbf{r})$ of valence electrons is uniform (with density n_0) inside the cylinder, and vanishing outside, i.e.

$$n(\mathbf{r}) = n_0\,\Theta\,(a-r)\,\Theta\left(\frac{L}{2}+z\right)\Theta\left(\frac{L}{2}-z\right), \tag{2.1}$$

where (r,θ,z) are the usual cylindrical coordinates, and where $\Theta(x)$ is the Heaviside step function.

Our strategy to obtain the frequencies of the plasmonic normal modes along the longitudinal ($\hat{z}$, $\alpha = \parallel$) and transverse ($\hat{r}$, $\alpha = \perp$) directions[1] closely follows the one presented, for example, in [22] for a spherical NP, which yields for the LSP resonance frequency the well-known Mie result $\omega_\mathrm{p}/\sqrt{3}$, with ω_p the plasma frequency.[2] We first impose a rigid shift $\mathbf{u}_\alpha$ of the electron distribution, which gives rise to the displaced density $n(\mathbf{r}-\mathbf{u}_\alpha)$. Assuming that $u_\alpha = |\mathbf{u}_\alpha|$ is small with respect to the dimensions of the cylinder, we have $n(\mathbf{r}-\mathbf{u}_\alpha) \simeq n(\mathbf{r}) + \delta n_\alpha(\mathbf{r})$, with

$$\delta n_\alpha(\mathbf{r}) = -\mathbf{u}_\alpha \cdot \nabla n(\mathbf{r}). \tag{2.2}$$

We then consider the resulting change in the Hartree energy (in cgs units)

$$\delta E_\alpha = \frac{e^2}{2}\int \mathrm{d}^3\mathbf{r}\int \mathrm{d}^3\mathbf{r}'\,\frac{\delta n_\alpha(\mathbf{r})\delta n_\alpha(\mathbf{r}')}{|\mathbf{r}-\mathbf{r}'|}, \tag{2.3}$$

with respect to the equilibrium situation. This quantity gives access to the restoring force

$$F_\alpha = -\frac{\partial}{\partial u_\alpha}(\delta E_\alpha) = -k_\alpha u_\alpha \tag{2.4}$$

and to the resulting spring constant k_α. The latter quantity then provides an expression for the normal mode frequency

$$\omega_{0,\alpha} = \sqrt{\frac{k_\alpha}{M_\mathrm{e}}}, \tag{2.5}$$

where $M_\mathrm{e} = N_\mathrm{e} m_\mathrm{e}$ corresponds to the total electronic mass.

Let us now consider the longitudinal ($\alpha = \parallel$) and transverse ($\alpha = \perp$) polarizations each in turn, which arise from different electronic distribution displacements $\mathbf{u}_\alpha$.

[1]Here and in what follows, hats designate unit vectors.

[2]Note that a similar phenomenological approach has been successfully applied by the authors of [63] to spin-dependent dipole excitations, and excellent agreement was obtained against time-dependent density functional theory numerical calculations.

(a) Longitudinal mode

We assume the longitudinal displacement $\mathbf{u}_\parallel = u\,\hat{z}$, such that the change in density (2.2) is

$$\delta n_\parallel(\mathbf{r}) = u n_0\, \Theta\,(a-r)\left[\delta\left(z-\frac{L}{2}\right)-\delta\left(z+\frac{L}{2}\right)\right], \tag{2.6}$$

where $\delta(x)$ is the Dirac delta function. Equation (2.6) corresponds to a charge imbalance that is located at the two disks of radius a closing the cylinder at $z=\pm L/2$ (cf. the inset in figure 1). In order to evaluate the modification of the Hartree energy (2.3) due to the above density change, we shall exploit the Laplace expansion of the Newtonian kernel [64]

$$\frac{1}{|\mathbf{r}-\mathbf{r}'|} = \frac{2}{\pi}\sum_{m=-\infty}^{+\infty}\int_0^\infty \mathrm{d}k\, \mathrm{e}^{\mathrm{i}m(\theta-\theta')}\cos\left(k[z-z']\right) I_m\,(kr_<)\, K_m\,(kr_>)\,. \tag{2.7}$$

Here, $I_m(x)$ and $K_m(x)$ are modified Bessel functions of the first and second kinds, respectively, while $r_< = \min(r,r')$ and $r_> = \max(r,r')$. Upon inserting (2.6) and (2.7) into (2.3), we arrive at a seven-dimensional integral. After carrying out the straightforward angular and Cartesian integrals, and using the following result for the double radial integral:

$$\int_0^a \mathrm{d}r\, r\int_0^a \mathrm{d}r'\, r' I_0\,(kr_<)\, K_0\,(kr_>) = \frac{a^2}{2k^2}\left[1-2I_1(ka)K_1(ka)\right], \tag{2.8}$$

we find

$$\delta E_\parallel = 8\pi(en_0u)^2a^3\int_0^\infty \frac{\mathrm{d}x}{x^2}\,\sin^2\left(\frac{L}{2a}x\right)\left[1-2I_1(x)K_1(x)\right], \tag{2.9}$$

which is harmonic in the displacement u. Evaluating the first term in the above integral using $\int_0^\infty \mathrm{d}t\,\sin^2(t)/t^2 = \pi/2$, and integrating the second term employing special functions, we find

$$\delta E_\parallel = 4\pi\,(eun_0)^2\,a^3\left[\frac{\pi L}{2a}+\frac{4}{3}-g\left(\frac{L}{a}\right)\right]. \tag{2.10}$$

In the expression above, the function $g(x)$ is defined as

$$g(x) = \frac{x}{6}\left[\left(x^2+4\right)K\left(-\frac{4}{x^2}\right)-\left(x^2-4\right)E\left(-\frac{4}{x^2}\right)\right], \tag{2.11}$$

where

$$K(x) = \int_0^1 \frac{\mathrm{d}t}{\sqrt{(1-t^2)(1-xt^2)}} \quad \text{and} \quad E(x) = \int_0^1 \mathrm{d}t\,\sqrt{\frac{1-xt^2}{1-t^2}} \tag{2.12}$$

are the complete elliptic integrals of the first and second kinds, respectively. The monotonically increasing function (2.11) has the following asymptotic expansions for small and large arguments:

$$g(x) \simeq \frac{4}{3}+(6\ln 2-1-2\ln x)\,\frac{x^2}{4}+\mathcal{O}(x^4), \quad x\ll 1 \tag{2.13a}$$

and

$$g(x) \simeq \frac{\pi}{2}\left(x+\frac{1}{2x}-\frac{1}{4x^3}\right)+\mathcal{O}(x^{-5}), \quad x\gg 1. \tag{2.13b}$$

The result (2.10), together with (2.4) and (2.5), then yields the following analytic expression for the resonance frequency of the dipolar longitudinal mode of the cylinder:

$$\omega_{0,\parallel} = \omega_\mathrm{p}\sqrt{1+\frac{2a}{\pi L}\left[\frac{4}{3}-g\left(\frac{L}{a}\right)\right]}. \tag{2.14}$$

Here, the plasma frequency of the considered metal is $\omega_\mathrm{p} = (4\pi n_0 e^2/m_\mathrm{e})^{1/2}$, with the electron density $n_0 = N_\mathrm{e}/\pi a^2 L$ for the examined cylinder.

We plot in figure 1*a* the longitudinal resonance frequency (2.14) as a function of the aspect ratio L/a of the cylinder as the solid red line. As one can see from the figure, $\omega_{0,\parallel}$ is a monotonically decreasing function of the parameter L/a, with the limiting values $\lim_{L/a\to 0}\{\omega_{0,\parallel}\} = \omega_\mathrm{p}$ and

$\lim_{L/a\to\infty}\{\omega_{0,\parallel}\}=0$, which coincide with the well-known asymptotic results for a spheroidal NP [11]. Physically, the longitudinal mode softens when the aspect ratio of the cylinder increases, since the ratio of uncompensated charges to the compensated ones (by the ionic background) decreases with increasing L/a. We note that this trend has been confirmed experimentally [16].

We now consider the two limiting cases of (2.14), namely when the cylinder can be treated as a nanodisk ($L/a \ll 1$) or a nanowire ($L/a \gg 1$), and where insightful expressions can be obtained. Let us first examine the disk limit. Using the expansion (2.13*a*), (2.14) becomes

$$\omega_{0,\parallel}^{\text{disk}} \simeq \omega_{\text{p}} \left\{1 - \frac{L}{4\pi a}\left[6\ln 2 - 1 - 2\ln\left(\frac{L}{a}\right)\right]\right\}, \quad \frac{L}{a} \ll 1. \tag{2.15}$$

Clearly, this expression tends linearly towards the plasma frequency ω_{p} in the extreme pancake limit ($L \to 0$); see the dashed green line in figure 1*a*. In the opposite limit of a wire, we obtain with (2.13*b*)

$$\omega_{0,\parallel}^{\text{wire}} \simeq \omega_{\text{p}}\sqrt{\frac{8a}{3\pi L}}, \quad \frac{L}{a} \gg 1, \tag{2.16}$$

which is plotted as a blue dotted line in figure 1*a*, showcasing the inverse square root decay to zero frequency.

(b) Transverse mode

In order to have access to the eigenfrequency of the transverse dipolar plasmonic mode, here we assume the arbitrary small displacement $\mathbf{u}_\perp = u\,\hat{x}$ (see the inset in figure 1), such that the change in electron density (2.2) is

$$\delta n_\perp(\mathbf{r}) = u n_0 \cos\theta\, \delta\,(r-a)\,\Theta\left(\frac{L}{2}+z\right)\Theta\left(\frac{L}{2}-z\right). \tag{2.17}$$

Completing an analogous calculation as to that for the preceding case of the longitudinally polarized mode (cf. §2a) leads to the following equation for the change in the Hartree energy (2.3):

$$\delta E_\perp = 8\pi (e n_0 u)^2 a^3 \int_0^\infty \frac{\mathrm{d}x}{x^2}\, \sin^2\left(\frac{L}{2a}x\right) I_1(x) K_1(x). \tag{2.18}$$

Evaluating the above integral then yields

$$\delta E_\perp = 2\pi\,(e u n_0)^2\, a^3 \left[g\left(\frac{L}{a}\right) - \frac{4}{3}\right], \tag{2.19}$$

where $g(x)$ is defined in (2.11). We thus obtain an analytic expression for the resonance frequency of the transverse dipolar plasmonic mode, using (2.4) and (2.5) with (2.19), as

$$\omega_{0,\perp} = \omega_{\text{p}}\sqrt{\frac{a}{\pi L}\left[g\left(\frac{L}{a}\right) - \frac{4}{3}\right]}. \tag{2.20}$$

We plot the transverse resonance frequency (2.20) in figure 1*b* as the solid red line, as a function of the aspect ratio L/a. As is evident from the figure, $\omega_{0,\perp}$ is a monotonically increasing function of the parameter L/a, bounded by the two limits $\lim_{L/a\to 0}\{\omega_{0,\perp}\}=0$ and $\lim_{L/a\to\infty}\{\omega_{0,\perp}\}=\omega_{\text{p}}/\sqrt{2}$ (the latter limit is denoted by the horizontal dash-dotted line in the figure). As is the case for the longitudinal plasmonic mode, such asymptotic limits are the same for a spheroidal NP [11]. Contrary to the longitudinal mode shown in figure 1*a*, the transverse mode gets harder when the aspect ratio of the cylinder increases, since the ratio of uncompensated charges that sit on the longitudinal surface of the cylinder to the compensated ones increases with increasing L/a.

In figure 1*b*, the limiting cases of a nanowire ($L/a \ll 1$, dashed green line) and nanodisk ($L/a \gg 1$, dotted blue line) are also displayed, and have functional forms which arise directly from (2.20)

with the leading order expansions (2.13). Explicitly, one finds

$$\omega_{0,\perp}^{\mathrm{disk}} \simeq \omega_{\mathrm{p}} \sqrt{\frac{L}{4\pi a}\left[6\ln 2 - 1 - 2\ln\left(\frac{L}{a}\right)\right]}, \quad \frac{L}{a} \ll 1 \tag{2.21}$$

and

$$\omega_{0,\perp}^{\mathrm{wire}} \simeq \frac{\omega_{\mathrm{p}}}{\sqrt{2}}\left(1 - \frac{4a}{3\pi L}\right), \quad \frac{L}{a} \gg 1. \tag{2.22}$$

(c) Discussion: comparison to spheroids, screening effects, and damping rates of the plasmonic resonances

In appendix A, we compare our analytical results (2.14) and (2.20) for the LSP resonance frequencies of a cylindrical NP to the closed-form expressions for a spheroidal particle with the same aspect ratio (e.g. [11]) and find an excellent agreement. Such a correspondence between both geometries as been previously pointed out by Venermo & Sihvola [65], who compared the polarizability of a cylinder calculated by means of numerical simulations to that of a spheroid, which is known analytically [11]. The comparison presented in appendix A thus confirms the relevance as well as the adequacy of our approach, which provides an analytical understanding of plasmonic modes for the cylinder geometry.

Thus far, our approach has neglected the possible dielectric screening of the valence electrons by the d electrons (characterized by a dielectric constant ϵ_{d}), which is of relevance for noble metal NPs, as well as the presence of a dielectric embedding medium (with constant ϵ_{m}). For the sphere geometry, the presence of screening and the resulting dielectric mismatch notoriously renormalizes [1] the Mie frequency from $\omega_{\mathrm{p}}/\sqrt{3}$ to $\omega_{\mathrm{p}}/(\epsilon_{\mathrm{d}} + 2\epsilon_{\mathrm{m}})^{1/2}$. Within our theoretical approach, it is straightforward to realize that when $\epsilon_{\mathrm{d}} \approx \epsilon_{\mathrm{m}} = \epsilon$, since the Hartree energy (2.3) is renormalized by a factor ϵ^{-1}, the resonance frequencies in (2.14) and (2.20) take on the same expressions, up to a replacement of ω_{p} by $\omega_{\mathrm{p}}/\sqrt{\epsilon}$, leading to a redshift of the resonances. The case $\epsilon_{\mathrm{d}} \neq \epsilon_{\mathrm{m}}$ is much more involved due to the complicated form of the Coulomb interaction in cylindrical coordinates, even within the wire limit [66], and is out of the scope of the present work.

A final comment is here in order about the damping of the plasmonic excitations which we have elucidated thus far. Metallic nano-objects are subject to radiative and non-radiative damping mechanisms which broaden the resonance of the collective excitation, such that the total decay rate of the LSP modes are given by $\gamma_\alpha = \gamma_\alpha^{\mathrm{r}} + \gamma^{\mathrm{nr}}$ ($\alpha = \parallel, \perp$). Within our dipolar approximation, the radiative decay rates $\gamma_\alpha^{\mathrm{r}}$ can be readily estimated from the electromagnetic field generated in the far-field by a point dipole [64] carrying a charge $-eN_{\mathrm{e}}$ and oscillating at the LSP resonance frequency $\omega_{0,\alpha}$. Evaluating the total power radiated by the dipole and the energy initially stored in it, we find

$$\gamma_\alpha^{\mathrm{r}} = \frac{\omega_{\mathrm{p}}^2 \omega_{0,\alpha}^2}{6c^3} a^2 L, \tag{2.23}$$

with c the speed of light in vacuum. The radiative damping rates $\gamma_\alpha^{\mathrm{r}}$ thus depend on the cylinder dimensions through the explicit dependence a^2L displayed by the equation above, but also through the aspect-ratio dependence of $\omega_{0,\alpha}$ (figure 1), and increases with the dimensions of the cylinder. Using the expansions (2.15), (2.16), (2.21) and (2.22), we find for the longitudinal mode $\gamma_\parallel^{\mathrm{r,disk}} \simeq \omega_{\mathrm{p}}^4 a^2 L/6c^3$ in the disk limit and $\gamma_\parallel^{\mathrm{r,wire}} \simeq 4\omega_{\mathrm{p}}^4 a^3/9\pi c^3$ in the wire limit, which, interestingly, does not depend on L, since $\omega_{0,\parallel}^{\mathrm{wire}}$ goes to zero for $L/a \gg 1$ (see (2.16)). For the transverse mode, we find $\gamma_\perp^{\mathrm{r,disk}} \simeq (6\ln 2 - 1)\omega_{\mathrm{p}}^4 a L^2/24\pi c^3$ and $\gamma_\perp^{\mathrm{r,wire}} \simeq \omega_{\mathrm{p}}^4 a^2 L/12c^3$.

The non-radiative contribution $\gamma^{\mathrm{nr}} = \gamma_{\mathrm{O}} + \gamma_{\mathrm{L}}$ to the total LSP linewidth, which is mode-independent in a first approximation, can be divided into two parts. The first part corresponds to the Ohmic, bulk-like contribution γ_{O} which essentially arises from electron–phonon and electron–electron scattering. The experiments on single gold nanorods protected by a silica shell of [16] report a value $\gamma_{\mathrm{O}} \approx 65\,\mathrm{meV}/\hbar$. The second part is the Landau damping decay rate γ_{L}, a purely quantum-mechanical effect [22,32] which comes from the confinement of the

electronic eigenstates within the NP, and which reads $\gamma_L = Av_F/\ell_{eff}$, with A a (material and dielectric environment-dependent) constant of order 1, v_F the Fermi velocity, and ℓ_{eff} an effective confinement length. The experiments of [16] have shown that $\ell_{eff} = (aL)^{1/2}$ provides a good fit to the measured data. In these experiments on individual gold nanorods having lengths L in between 32 nm and 70 nm and radii a in the range 4.3 nm to 11 nm, Landau damping was shown to largely dominate the size-dependent part of the total linewidth (which is in the 80–140 meV/$\hbar$ range), while the maximal value of the radiative damping decay rate reported is only 15 meV/$\hbar$.

3. Frequency renormalization due to the spill-out effect

So far, our approach has been purely classical, and has neglected the spill out of the electronic wave functions outside of the NP. This approximation follows from our assumed hard wall mean-field potential, resulting in the approximate density of valence electrons given by (2.1). However, the quantum-mechanical spill-out effect is known to renormalize the LSP resonance frequencies, and is particularly prominent for NPs of only a few nanometres in size [32]. We thus relax the above hard-wall approximation, and assume that the mean-field potential (including both the ionic positive background and the electron–electron interactions) seen by the valence electrons of the NP is given by

$$V(\mathbf{r}) = V_0\,\Theta\,(r-a)\,\Theta\left(|z| - \frac{L}{2}\right), \tag{3.1}$$

where $V_0 = \epsilon_F + W$ is the height of the potential, with ϵ_F and W the Fermi energy and the work function of the NP, respectively. Such a hypothesis has been tested using density functional *ab initio* calculations using the local density approximation in [67], and is a fairly good approximation to the realistic mean-field potential.

Due to the finite height V_0 of the mean-field potential (3.1), some part of the valence electrons can spill out of the cylindrical NP, effectively increasing its length and radius according to the replacements

$$L \to \tilde{L} = L + 2\ell_\parallel, \quad a \to \tilde{a} = a + \ell_\perp. \tag{3.2}$$

Here, the small spill-out lengths $\ell_\parallel \ll L$ and $\ell_\perp \ll a$ in the longitudinal ($\hat{z}$) and transverse ($\hat{r}$) directions, respectively, can be estimated from the average number of spill-out electrons $\mathcal{N}_\parallel$ and $\mathcal{N}_\perp$ in both of these directions according to

$$\ell_\parallel = \frac{1}{2}\frac{\mathcal{N}_\parallel}{N_e}L \quad \text{and} \quad \ell_\perp = \frac{1}{2}\frac{\mathcal{N}_\perp}{N_e}a. \tag{3.3}$$

In the following, we will estimate $\mathcal{N}_\parallel$ and $\mathcal{N}_\perp$ using semiclassical expansions, which will give us access to the spill-out lengths $\ell_\parallel$ and $\ell_\perp$. We will then incorporate the prescription (3.2) into the mode frequencies (2.14) and (2.20), which will then provide us with an estimate of the renormalized resonance frequencies.

(a) Average number of spill-out electrons and spill-out lengths

At zero temperature, the average numbers of spill-out electrons in the longitudinal and transverse directions are given by

$$\mathcal{N}_\parallel = \sum_\lambda^{\text{occ}} \int_{\substack{r<a \\ |z|>L/2}} \mathrm{d}^3\mathbf{r}\;|\psi_\lambda(\mathbf{r})|^2 \quad \text{and} \quad \mathcal{N}_\perp = \sum_\lambda^{\text{occ}} \int_{\substack{r>a \\ |z|<L/2}} \mathrm{d}^3\mathbf{r}\;|\psi_\lambda(\mathbf{r})|^2, \tag{3.4}$$

respectively. Here, λ labels the bound states in the mean-field potential (3.1) and the summations run over occupied states up to the Fermi level. The single-particle wave function $\psi_\lambda(\mathbf{r})$ obeys the

time-independent Schrödinger equation

$$\left[-\frac{\hbar^2}{2m_\mathrm{e}}\nabla^2 + V(\mathbf{r})\right]\psi_\lambda(\mathbf{r}) = \epsilon_\lambda\psi_\lambda(\mathbf{r}), \tag{3.5}$$

with ϵ_λ the corresponding eigenenergies. Note that in (3.4), we disregard the negligible number of spill-out electrons arising at the corners of the cylindrical NP.

The choice of mean-field potential (3.1) leads to a non-separable Schrödinger equation (3.5). However, the replacement

$$V(\mathbf{r}) \simeq V_0\left[\Theta\,(r-a) + \Theta\left(|z| - \frac{L}{2}\right)\right] \tag{3.6}$$

is both an excellent approximation for the original $V(\mathbf{r})$, with only the corners of the cylinder deviating from the non-separable potential (3.1), and leads to an exactly solvable problem. Decomposing the separable potential (3.6) into $V(\mathbf{r}) = V_r(r) + V_z(z)$ with $V_r(r) = V_0\Theta(r-a)$ and $V_z(z) = V_0\Theta(|z| - L/2)$, the stationary Schrödinger equation (3.5) then reads

$$\left\{\frac{\partial^2}{\partial r^2} + \frac{1}{r}\frac{\partial}{\partial r} + \frac{1}{r^2}\frac{\partial^2}{\partial\theta^2} + \frac{\partial^2}{\partial z^2} + k^2 - \frac{2m_\mathrm{e}}{\hbar^2}\left[V_r(r) + V_z(z)\right]\right\}\psi_{nm\tilde{n}}(\mathbf{r}) = 0, \tag{3.7}$$

where $k = \sqrt{2m_\mathrm{e}\epsilon/\hbar^2}$, and where m is the magnetic quantum number and n ($\tilde{n}$) is the principal quantum number due to the transverse (longitudinal) motion. We separate the variables in (3.7) using

$$\psi_{nm\tilde{n}}(\mathbf{r}) = F_{nm}(r,\theta)Z_{\tilde{n}}(z), \tag{3.8}$$

and are thus led to two Schrödinger equations in the reduced eigenvalues k_r and k_z, respectively, where $k^2 = k_r^2 + k_z^2$, whose solutions are given explicitly in appendix B. Using the results presented there (see in particular (B 10)), we are then able to evaluate the integrals entering (3.4), which are approximately given in the high-energy, semiclassical limit of $k_0 a \gg 1$ and $k_0 L \gg 1$ (with $k_0 = (2m_\mathrm{e}V_0/\hbar^2)^{1/2}$) by

$$\int_{\substack{r<a\\|z|>L/2}} \mathrm{d}^3\mathbf{r}\;\left|\psi_{nm\tilde{n}}(\mathbf{r})\right|^2 \simeq \frac{2}{\kappa_z L}\frac{k_z^2}{k_0^2} \quad\text{and}\quad \int_{\substack{r>a\\|z|<L/2}} \mathrm{d}^3\mathbf{r}\;\left|\psi_{nm\tilde{n}}(\mathbf{r})\right|^2 \simeq \frac{1}{2\kappa_r a}, \tag{3.9}$$

where $\kappa_r = (k_0^2 - k_r)^{1/2}$ and $\kappa_z = (k_0^2 - k_z)^{1/2}$.

Upon substituting the expressions (3.9) into (3.4), we then replace the summation over the set of quantum numbers n, m and $\tilde{n}$ by an integral over wave vector $\mathbf{k}$. We take for the density of states the leading-in-$\hbar$ Weyl term [68], which is appropriate in the semiclassical limit $k_\mathrm{F} a \gg 1$ and $k_\mathrm{F} L \gg 1$ (with k_F the Fermi wave vector). For typical noble metals, such as Ag or Au, one has $k_\mathrm{F} a \simeq 10\,a$[nm], so that the semiclassical approximation is suitable even for nanometre-sized NPs [69]. The aforementioned prescription leads to

$$\mathcal{N}_\parallel \simeq 2\frac{V}{(2\pi)^3}\int_{k<k_\mathrm{F}} \mathrm{d}^3\mathbf{k}\,\frac{2}{\kappa_z L}\frac{k_z^2}{k_0^2} \quad\text{and}\quad \mathcal{N}_\perp \simeq 2\frac{V}{(2\pi)^3}\int_{k<k_\mathrm{F}} \mathrm{d}^3\mathbf{k}\,\frac{1}{2\kappa_r a}, \tag{3.10}$$

where the prefactor of 2 accounts for the spin degeneracy and $V = \pi a^2 L$ is the volume of the cylinder. Performing the above integrals in spherical coordinates, we arrive at

$$\mathcal{N}_\parallel = \frac{k_0^2 a^2}{\pi}\int_0^{k_\mathrm{F}/k_0} \mathrm{d}x\,x^4 \int_{-1}^{+1}\mathrm{d}t\,\frac{t^2}{\sqrt{1-x^2t^2}} \quad\text{and}\quad \mathcal{N}_\perp = \frac{k_0^2 aL}{4\pi}\int_0^{k_\mathrm{F}/k_0}\mathrm{d}x\,x^2\int_{-1}^{+1}\mathrm{d}t\,\frac{1}{\sqrt{1-x^2(1-t^2)}}, \tag{3.11}$$

where $k_0 > k_\mathrm{F}$, and where the integrals with respect to the dimensionless radial (x) and polar (t) coordinates are yet to be performed. Evaluating the above integrals (3.11), we find the expressions

$$\mathcal{N}_\parallel = \frac{(k_\mathrm{F}a)^2}{4\pi}h_\parallel\left(\frac{\epsilon_\mathrm{F}}{V_0}\right) \quad\text{and}\quad \mathcal{N}_\perp = \frac{k_\mathrm{F}^2 aL}{4\pi}h_\perp\left(\frac{\epsilon_\mathrm{F}}{V_0}\right). \tag{3.12}$$

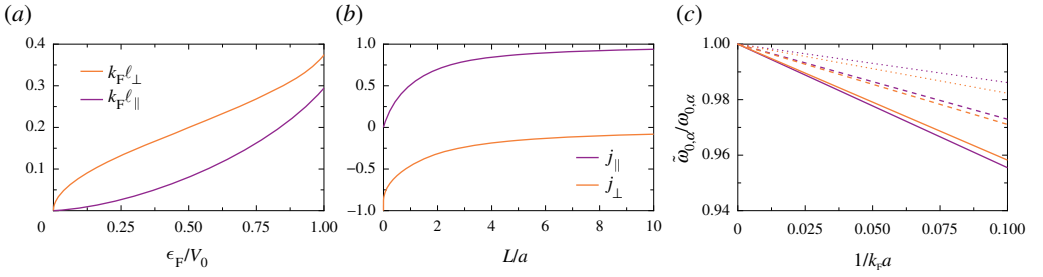

Figure 2. (*a*) Spill-out lengths (3.15), scaled with the Fermi wave vector k_F, as a function of the ratio of the Fermi energy to mean-field potential strength, ϵ_F/V_0. (*b*) Auxiliary functions j_α ($\alpha = \parallel, \perp$) from (3.17) as a function of the aspect ratio L/a. (*c*) Renormalized resonance frequencies $\tilde{\omega}_{0,\parallel}$ (violet lines) and $\tilde{\omega}_{0,\perp}$ (orange lines) from (3.16) in units of the bare frequencies $\omega_{0,\alpha}$ as a function of the inverse size of the nanoparticle (dotted lines: $\epsilon_F/V_0 = 0.25$; dashed lines: $\epsilon_F/V_0 = 0.50$; solid lines: $\epsilon_F/V_0 = 0.75$), for $L/a = 1$. (Online version in colour.)

Here, we have introduced the auxiliary functions

$$h_\parallel(x) = \left(\frac{3}{2} - x\right)\sqrt{\frac{1}{x} - 1} + \left(2 - \frac{3}{2x}\right)\arcsin\sqrt{x} \quad \text{and} \quad h_\perp(x) = \frac{1}{\sqrt{x}} + \left(1 - \frac{1}{x}\right)\operatorname{arctanh}\sqrt{x}. \tag{3.13}$$

Scaling the results (3.12) with the total number of electrons in the NP $N_e = La^2k_F^3/3\pi$, we obtain

$$\frac{\mathcal{N}_\parallel}{N_e} = \frac{3}{4k_FL}h_\parallel\left(\frac{\epsilon_F}{V_0}\right) \quad \text{and} \quad \frac{\mathcal{N}_\perp}{N_e} = \frac{3}{4k_Fa}h_\perp\left(\frac{\epsilon_F}{V_0}\right). \tag{3.14}$$

Thus, the fraction of spill-out electrons in both the longitudinal and transverse directions scales with the inverse of the spatial extent of the cylinder ($\propto 1/a$, $1/L$), and so becomes increasingly important for particles with nanometric dimensions.

With the above results (3.14), we can now evaluate the spill-out lengths (3.3), which read

$$k_F\ell_\parallel = \frac{3}{8}h_\parallel\left(\frac{\epsilon_F}{V_0}\right) \quad \text{and} \quad k_F\ell_\perp = \frac{3}{8}h_\perp\left(\frac{\epsilon_F}{V_0}\right). \tag{3.15}$$

Importantly, these two quantities do not depend on the NP dimensions L and a, and only on the Fermi energy ϵ_F (or the Fermi wave vector k_F) and the depth V_0 of the mean-field potential (3.1). The spill-out lengths (3.15) are plotted in figure 2*a* as a function of ϵ_F/V_0. As one can see from the figure, both of these quantities smoothly increase with the above-mentioned ratio. Since k_F is typically of the order of $10^8\,\mathrm{cm}^{-1}$ for alkaline or noble metals, and since ϵ_F/V_0 is roughly of the order of 0.5 [32], the spill-out lengths (3.15) are only of a few tenths of an angstrom. However, as we will see in the next section, such a tiny spread of the electronic wave functions outside of the NP may have a non-negligible effect on the LSP resonance frequency.

(b) Frequency redshifts due to the spill-out effect

We are now in a position to calculate the renormalized resonance frequency in the longitudinal (transverse) polarization $\tilde{\omega}_{0,\parallel}$ ($\tilde{\omega}_{0,\perp}$) due to the spill-out effect. We account for the spill-out of the electrons by treating the cylindrical NP with the effective dimensions $\tilde{L}$ and $\tilde{a}$ as in (3.2). It follows from the direct substitution of these effective dimensions into the resonance frequencies (2.14) and (2.20), which assumed hard-wall confinement of the valence electrons, that the renormalized resonance frequencies are, to leading order in the scaled spill-out lengths $\ell_\parallel/L$ and $\ell_\perp/a$ (cf. (3.15)), given by

$$\tilde{\omega}_{0,\alpha} \simeq \omega_{0,\alpha}\left\{1 - \left[1 + j_\alpha\left(\frac{L}{a}\right)\right]\frac{\ell_\parallel}{L} - \left[1 - \frac{1}{2}j_\alpha\left(\frac{L}{a}\right)\right]\frac{\ell_\perp}{a}\right\}, \quad \alpha = \parallel, \perp. \tag{3.16}$$

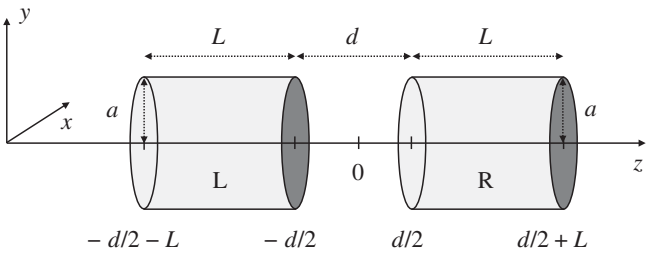

Figure 3. Sketch of a dimer of cylindrical metallic nanoparticles, denoted L and R. Each nanoparticle is of radius a and length L, and they are separated by an end-to-end gap distance d. (Online version in colour.)

Here, we defined the two functions

$$j_{\parallel}(x) = \frac{(2/\pi x)\left[4/3 - g(x) + xg'(x)\right]}{1 + (2/\pi x)[4/3 - g(x)]} \quad \text{and} \quad j_{\perp}(x) = \frac{4/3 - g(x) + xg'(x)}{4/3 - g(x)}, \tag{3.17}$$

where

$$g'(x) = \frac{1}{2}\left[\left(x^2 + 4\right) K\left(-\frac{4}{x^2}\right) - x^2 E\left(-\frac{4}{x^2}\right)\right] \tag{3.18}$$

is the derivative with respect to x of the function $g(x)$ defined in (2.11).

We plot in figure 2*b* the auxiliary functions (3.17), which are both monotonically increasing functions of the aspect ratio L/a of the cylinder sketched in the inset of figure 1, with $0 < j_{\parallel} < 1$ and $-1 < j_{\perp} < 0$. Thus, the prefactors of the terms $\propto 1/L$ and $\propto 1/a$ in (3.16) are negative, such that the LSP resonance frequencies of the cylinder experience a redshift as the NP size decreases, as is the case for the sphere geometry [32]. This is exemplified in figure 2*c*, which displays the renormalized resonance frequencies (3.16) (in units of the bare ones) as a function of $1/k_{\mathrm{F}}a$, for an aspect ratio $L/a = 1$, and for increasing values of $\epsilon_{\mathrm{F}}/V_0$. As one can see from the figure, the deviation due to the spill-out effect from the bare resonance frequencies can reach between *ca* 1.5% and 4.5% (depending on the ratio $\epsilon_{\mathrm{F}}/V_0$, which is essentially material-dependent) for $k_{\mathrm{F}}a = 10$ (which typically corresponds to $a \simeq 1$ nm for normal metals). Progress in nanofabrication techniques should allow one to vary the cylindrical NP size and thus to measure the predicted size dependence of the resonance frequencies (3.16).

4. Coupled modes in a cylindrical dimer

We now consider a dimer of cylindrical NPs composed of the same metal, which are aligned along the z-axis, and are separated by a distance d (figure 3). The two cylinders, denoted left (L) and right (R), are both of a radius a and length L, and contain N_{e} valence electrons each. In the following, we study the resultant coupled plasmonic modes in the dimer, for both the longitudinal ($\alpha = \parallel$) and transverse ($\alpha = \perp$) polarizations, in a similar fashion to the single-cylinder calculation of §2.

Notably, we focus on the dipolar modes and do not take into account higher-order contributions to the collective plasmon–plasmon interactions, which are only relevant for small interparticle separations.[3] We also focus on separation distances such that the near-field coupling between the LSPs on each NP dominates, and thus disregard retardation effects. The latter only lead to small frequency renormalization effects in NP dimers [71] (although retardation effects can be significant in long NP chains [47,72,73]).

We start by neglecting the spill-out of the electronic wave functions outside of each cylinder. As in §2, we assume that the density $n(\mathbf{r})$ of valence electrons is uniform within each cylinder

[3]For spheres, this non-dipolar regime is given by $s \lesssim 3R$, where R is the NP radius and s is the point-to-point separation [70].

(with density n_0), and vanishing outside. We thus have

$$n(\mathbf{r}) = n_{\mathrm{L}}(\mathbf{r}) + n_{\mathrm{R}}(\mathbf{r}), \tag{4.1}$$

where, in cylindrical coordinates, the single NP contributions are

$$n_{\mathrm{L}}(\mathbf{r}) = n_0\, \Theta\,(a-r)\, \Theta\left(-z-\frac{d}{2}\right) \Theta\left(L+\frac{d}{2}+z\right) \tag{4.2a}$$

and

$$n_{\mathrm{R}}(\mathbf{r}) = n_0\, \Theta\,(a-r)\, \Theta\left(z-\frac{d}{2}\right) \Theta\left(L+\frac{d}{2}-z\right). \tag{4.2b}$$

In order to have access to the frequencies of the coupled dipolar modes, we shall impose two types of rigid displacements $\mathbf{u}_\alpha^\tau$ on the total density (4.1) for each polarization α, distinguished by the index $\tau = \pm$. To first order in the displacement field $\mathbf{u}_\alpha^\tau$, the electronic density is perturbed like $n(\mathbf{r}-\mathbf{u}_\alpha^\tau) \simeq n(\mathbf{r}) + \delta n_\alpha^\tau(\mathbf{r})$, where

$$\delta n_\alpha^\tau(\mathbf{r}) = -\mathbf{u}_\alpha^\tau \cdot \nabla n(\mathbf{r}). \tag{4.3}$$

This density change gives rise to the two possible normal modes of the system (labelled by τ) for each polarization α, which we now consider in turn.

(a) Longitudinal modes

Firstly, let us consider the symmetric mode in the longitudinal polarization ($\rightarrow\rightarrow$), which we denote with the index $\tau = -$ since it constitutes the low-energy mode. We enforce the displacement $\mathbf{u}_\parallel^- = u\,\hat{z}$ in both cylinders, such that the shift in density (4.3) is $\delta n_\parallel^-(\mathbf{r}) = \delta n_{\mathrm{L},\parallel}(\mathbf{r}) + \delta n_{\mathrm{R},\parallel}(\mathbf{r})$, with

$$\delta n_{\mathrm{L},\parallel}(\mathbf{r}) = u n_0\, \Theta\,(a-r) \left[\delta\left(z+\frac{d}{2}\right) - \delta\left(L+\frac{d}{2}+z\right)\right] \tag{4.4a}$$

and

$$\delta n_{\mathrm{R},\parallel}(\mathbf{r}) = u n_0\, \Theta\,(a-r) \left[\delta\left(L+\frac{d}{2}-z\right) - \delta\left(z-\frac{d}{2}\right)\right]. \tag{4.4b}$$

Secondly, let us consider the antisymmetric, high-energy mode ($\rightarrow\leftarrow$), which we mark with the index $\tau = +$. Imposing the rigid displacements $\mathbf{u}_\parallel^+ = \pm u\,\hat{z}$, which act in different directions ($\pm$) in each cylinder (L relative to R), the change in density (4.3) reads $\delta n_\parallel^+(\mathbf{r}) = \delta n_{\mathrm{R},\parallel}(\mathbf{r}) - \delta n_{\mathrm{L},\parallel}(\mathbf{r})$, in terms of the quantities (4.4).

The change in electrostatic interactions between the electronic clouds is described by the change in the Hartree energy

$$\delta E_\parallel^\tau = \delta E_\parallel^{\mathrm{LL}} + \delta E_\parallel^{\mathrm{RR}} - \tau\left(\delta E_\parallel^{\mathrm{LR}} + \delta E_\parallel^{\mathrm{RL}}\right), \tag{4.5}$$

where we have used the decomposition

$$\delta E_\alpha^{ij} = \frac{e^2}{2} \int \mathrm{d}^3\mathbf{r} \int \mathrm{d}^3\mathbf{r}' \frac{\delta n_{i,\alpha}(\mathbf{r})\delta n_{j,\alpha}(\mathbf{r}')}{|\mathbf{r}-\mathbf{r}'|}, \tag{4.6}$$

where $i,j \in \{\mathrm{L},\mathrm{R}\}$, $\alpha \in \{\parallel,\perp\}$ and $\delta n_{i,\parallel}(\mathbf{r})$ are given in (4.4). The first two terms on the right-hand side of (4.5) describe the contributions from each cylinder in isolation, $\delta E_\parallel^{\mathrm{LL}} = \delta E_\parallel^{\mathrm{RR}} = \delta E_\parallel$, where $\delta E_\parallel$ is given in (2.10). The effect of electrostatic coupling is contained in the final two terms of (4.5). An analogous calculation to that which led to (2.10) yields for the remaining two terms in (4.5) the expression

$$\delta E_\parallel^{\mathrm{LR}} = \delta E_\parallel^{\mathrm{RL}} = 2\pi\,(eun_0)^2\, a^3 \left[2g\left(\frac{L+d}{a}\right) - g\left(\frac{d}{a}\right) - g\left(\frac{2L+d}{a}\right)\right], \tag{4.7}$$

where the function $g(x)$ is defined in (2.11).

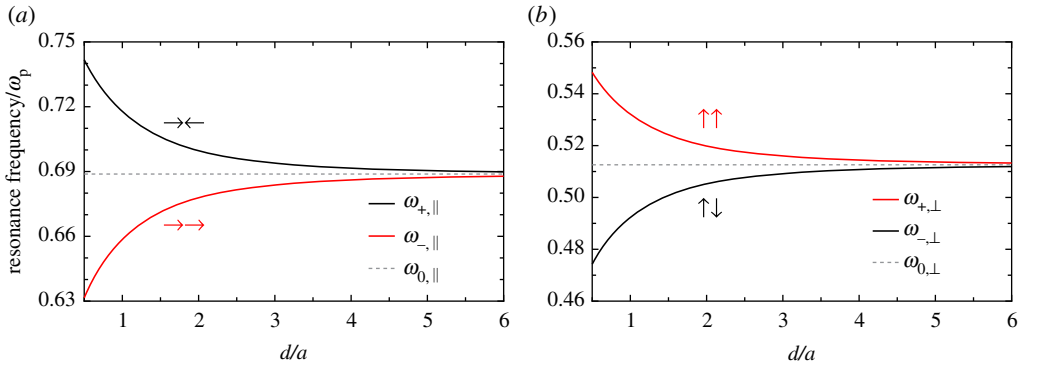

Figure 4. Resonance frequencies of the dark (black lines) and bright (red lines) coupled modes, in units of the plasma frequency ω_p, as a function of interparticle separation d, in units of the cylinder radius a. (*a*) Longitudinal modes $\omega_{\tau,\parallel}$, as encapsulated by (4.8), and the associated single NP result $\omega_{0,\parallel}$ from (2.14). (*b*) Transverse modes $\omega_{\tau,\perp}$, as given by (4.13), and the corresponding single NP result $\omega_{0,\perp}$ from (2.20). In the figure, the aspect ratio $L/a = 1$. (Online version in colour.)

The restoring force $F_\alpha^\tau = -\partial_u(\delta E_\alpha^\tau) = -k_\alpha^\tau u$ then provides us with a relation to the effective spring constant k_α^τ of the problem, from which the resonance frequencies $\omega_{\tau,\alpha} = \sqrt{k_\alpha^\tau/2N_e m_e}$ are revealed.[4] Hence the longitudinal eigenfrequencies of a dimer of cylindrical NPs are given by

$$\omega_{\tau,\parallel} = \sqrt{\omega_{0,\parallel}^2 + 2\tau\Omega^2}, \tag{4.8}$$

which accounts for both the high-energy ($\tau = +, \rightarrow\leftarrow$) and the low-energy ($\tau = -, \rightarrow\rightarrow$) modes. Here, $\omega_{0,\parallel}$ is the resonance frequency of an isolated cylinder (2.14), which depends on the aspect ratio L/a, while the effective coupling constant of the problem Ω has the functional form

$$\Omega = \omega_p\sqrt{\frac{a}{2\pi L}\left[g\left(\frac{d}{a}\right) + g\left(\frac{2L+d}{a}\right) - 2g\left(\frac{L+d}{a}\right)\right]} \tag{4.9}$$

and depends on both L/a and d/a. Equation (4.8) analytically describes the longitudinal resonance frequencies of the pair of coupled dipolar modes of the cylindrical dimer, provided the separation d is not too small (i.e. where one can neglect multipolar effects and/or the quantum tunnelling of electrons between the two NPs comprising the dimer).

Interestingly, we show in appendix C that the result (4.8), in the limit of large interparticle distance (i.e. $d/a \gg 1$ and $d/L \gg 1$), for which we have (using (2.13*b*))

$$\Omega \simeq \omega_p\sqrt{\frac{La^2}{4d^3}}, \tag{4.10}$$

can be found from a simple model of coupled point dipoles. From (4.10), one further immediately notices that in the extreme isolation limit ($d \to \infty$), the coupling constant (4.9) vanishes and thus the single NP resonance frequency (2.14) is recovered by (4.8).

We plot the dimer resonance frequencies (4.8) as a function of the interparticle separation d in figure 4*a*, for both the high-energy (black line) and the low-energy (red line) modes, for the aspect ratio $L/a = 1$. Evidently, for separations of just a few multiples of the cylinder size, the two resonance frequencies converge onto the one of a single cylinder $\omega_{0,\parallel}$ (see the grey dashed line). As one can see from the figure, for separations below the cylinder size, the pair of plasmonic levels become increasingly distinct and hence experimentally detectable. The bright mode ($\rightarrow\rightarrow$) may be accessed optically, whereas the dark mode ($\rightarrow\leftarrow$) should be probed via electron energy loss spectroscopy (EELS) [8].

[4]Note that $2N_e m_e$ corresponds to the total electronic mass of the dimer.

For completeness, we now consider the two limiting cases of equation (4.8), i.e. the nanodisk ($L/a \ll 1$) and nanowire ($L/a \gg 1$) limits, and for large separation distances ($d/a \gg 1$, $d/L \gg 1$). Using (4.10), the full eigenspectrum (4.8) of the coupled nanodisks reads $\omega^{\text{disk}}_{\tau,\parallel} \simeq \omega^{\text{disk}}_{0,\parallel} + \tau\omega_{\text{p}}(La^2/4d^3)$, where $\omega^{\text{disk}}_{0,\parallel}$ is given in (2.15), analytically demonstrating the expected inverse cubic decay with separation ($\propto 1/d^3$), which is characteristic of a quasi-static dipolar interaction [64]. In the opposite regime of a dimer of wire-like NPs, and further assuming $L^2a/d^3 \ll 1$, we have $\omega^{\text{wire}}_{\tau,\parallel} \simeq \omega^{\text{wire}}_{0,\parallel} + \tau(\omega_{\text{p}}/8)\sqrt{3\pi/2}\left(\frac{\sqrt{La}}{d}\right)^3$, where an expression for $\omega^{\text{wire}}_{0,\parallel}$ can be found in (2.16), again showcasing the characteristic scaling typical of the dipole–dipole interaction regime ($\propto 1/d^3$).

(b) Transverse modes

The calculation for the transverse polarized coupled modes ($\alpha = \perp$) proceeds in a similar manner to that of the previous subsection. The main difference is that the symmetric mode ($\uparrow\uparrow$) is now the high-energy mode and is associated with $\tau = +$, while the antisymmetric mode ($\uparrow\downarrow$) corresponds to the low-energy mode and has the label $\tau = -$.

We again consider two separate displacements in order to characterize the two coupled dipolar modes. Firstly, we assume $\mathbf{u}^{+}_{\perp} = u\,\hat{x}$, which gives rise to the symmetric mode, and secondly we let $\mathbf{u}^{-}_{\perp} = \pm u\,\hat{x}$, which distinguishes the antisymmetric mode (in the right-hand side of $\mathbf{u}^{-}_{\perp}$, the $\pm$ refers to the displacements being in opposite directions for cylinder L as compared to R). The shift in electronic density across the dimer then reads $\delta n^{\tau}_{\perp}(\mathbf{r}) = \delta n_{\text{L},\perp}(\mathbf{r}) + \tau\delta n_{\text{R},\perp}(\mathbf{r})$, where

$$\delta n_{\text{L},\perp}(\mathbf{r}) = un_0\,\cos\theta\,\delta\,(a-r)\,\Theta\left(-z-\frac{d}{2}\right)\Theta\left(L+\frac{d}{2}+z\right) \tag{4.11a}$$

and

$$\delta n_{\text{R},\perp}(\mathbf{r}) = un_0\,\cos\theta\,\delta\,(a-r)\,\Theta\left(z-\frac{d}{2}\right)\Theta\left(L+\frac{d}{2}-z\right), \tag{4.11b}$$

as follows from (4.2) and (4.3).

The change in Hartree energy accounts for the transverse electrostatic interactions via $\delta E^{\tau}_{\perp} = \delta E^{\text{LL}}_{\perp} + \delta E^{\text{RR}}_{\perp} + \tau(\delta E^{\text{LR}}_{\perp} + \delta E^{\text{RL}}_{\perp})$, where we used the decomposition of (4.6). The first two terms in $\delta E^{\tau}_{\perp}$ are single NP contributions, and so are exactly that of (2.19), explicitly $\delta E^{\text{LL}}_{\perp} = \delta E^{\text{RR}}_{\perp} = \delta E_{\perp}$. The remaining coupling terms in $\delta E^{\tau}_{\perp}$ are also equal by symmetry, and are given by

$$\delta E^{\text{LR}}_{\perp} = \delta E^{\text{RL}}_{\perp} = \pi\,(eun_0)^2\,a^3\left[g\left(\frac{d}{a}\right) + g\left(\frac{2L+d}{a}\right) - 2g\left(\frac{L+d}{a}\right)\right], \tag{4.12}$$

where $g(x)$ was introduced in (2.11). As in the previous subsection, the analytic expression for the transverse resonance frequencies soon follows from the restoring force $F^{\tau}_{\perp}$ (see below (4.7) for details) as

$$\omega_{\tau,\perp} = \sqrt{\omega^2_{0,\perp} + \tau\Omega^2}, \tag{4.13}$$

where the coupling constant Ω is defined in (4.9), and with the single cylinder resonance frequency $\omega_{0,\perp}$ of (2.20). Notably, compared to the longitudinal result $\omega_{\tau,\parallel}$ of (4.8), the second term under the square root in (4.13), the so-called coupling term, is half as large. This property is familiar from the canonical case of a dimer of spherical NPs, where the longitudinal modes are also (approximately) twice as widely split as the transverse modes [52,71]. Moreover, we note that in the limit of large interparticle distance, the result (4.13) can be inferred from the coupled point dipole model discussed in appendix C.

The transverse polarized dimer resonance frequencies (4.13) are plotted as a function of the interparticle separation d in figure 4*b*, with the aspect ratio fixed at $L/a = 1$. The plot illustrates increasingly large inter-mode splittings for decreasing separations d, such that $\omega_{\tau,\perp}$ become significantly detuned from the single cylinder result (dashed grey line). In stark contrast to the longitudinal coupled modes of figure 4*a*, in figure 4*b* it is the high-energy mode which strongly couples to light (red line), and as such may be detected straightforwardly by optical means, while the low-energy mode is dark (black line), and as such requires EELS probing techniques.

A remark is now in order about the influence of the spill-out effect on the coupled mode frequencies shown in figure 4. Since the effective coupling constant Ω of (4.9) already represents a rather small correction to the single particle results $\omega_{0,\parallel}$ and $\omega_{0,\perp}$ in (4.8) and (4.13), respectively, we can safely assume that Ω is not renormalized by the spill-out lengths (3.15). Therefore, the renormalized coupled mode frequencies are $\tilde{\omega}_{\tau,\parallel} = (\tilde{\omega}_{0,\parallel}^2 + 2\tau\Omega^2)^{1/2}$ and $\tilde{\omega}_{\tau,\perp} = (\tilde{\omega}_{0,\perp}^2 + \tau\Omega^2)^{1/2}$ respectively, where $\tilde{\omega}_{0,\parallel}$ and $\tilde{\omega}_{0,\perp}$ are given in (3.16). Henceforth, the only effect of the spill-out electrons is a global frequency shift towards the red end of the spectrum, which does not depend on the interparticle distance d.

We conclude this section by commenting on the linewidth of the coupled LSP modes which we have calculated. While the non-radiative part (i.e. Ohmic and Landau damping) does not depend in first approximation on the bright or dark nature of the mode and can be evaluated from the single-particle result discussed in §2c [52], the radiative part is strongly mode-dependent. Indeed, dark modes in dimers of near-field coupled NPs essentially do not radiate and are immune to radiation damping, while the damping rate of the bright modes is approximately given by twice the result (2.23) for an individual NP.

5. Conclusion

We have considered the fundamental problem of characterizing analytically within the quasi-static approximation the longitudinal and transverse dipolar modes supported by a cylindrical NP with an arbitrary aspect ratio. Inspired by the trend of increasing miniaturization, we have derived semiclassical expressions for the spill-out lengths in metallic cylinders, and have shown that this quantum phenomenon can significantly renormalize the plasmonic frequencies. Recent experiments on plasmonic cylinders, including with nanodisks and nanowires, suggest that both the resonance frequency dependence on the cylinder aspect ratio and the quantum size effect we consider may be probed in cutting edge laboratories [15–21].

We have also developed an analytical theory of a dimer of cylindrical NPs, and have derived a simple expression for the bright and dark mode eigenfrequencies of the collective plasmons, for both the longitudinal and transverse polarizations. These results provide insight into the evolution of the splitting of the coupled modes as a function of the interparticle separation, and act as a benchmark for future experimental and numerical studies of collective plasmonic behaviour [35,50,51].

Data accessibility. This article has no additional data.

Authors' contributions. C.A.D. and G.W. performed the analytical calculations. C.A.D. wrote a first version of the manuscript, which was finalized by G.W. The project was supervised by G.W. Both authors gave final approval for publication and agree to be held accountable for the work performed therein.

Competing interests. We declare we have no competing interests.

Funding. We acknowledge support from Agence Nationale de la Recherche (grant no. ANR-14-CE26-0005 Q-MetaMat). C.A.D. acknowledges support from the Juan de la Cierva programme (MINECO, Spain) and from the Royal Society University Research Fellowship (URF/R1/201158). This research project has been supported by the University of Strasbourg IdEx programme.

Acknowledgements. We thank Adam Brandstetter-Kunc, Rodolfo A. Jalabert and Dietmar Weinmann for stimulating discussions.

Appendix A. Comparison between cylinders and spheroids

The list of analytic expressions describing the electrostatic response of NPs of different geometries is commonly thought to be limited to spheres and ellipsoids [11]. Perhaps surprisingly, and certainly unfortunately due to the experimental ubiquity of cylindrical nanorods, the plasmonic modes of cylinders cannot be found analytically via the typical route of solving Laplace's equation, finding the polarizability of the oscillating dipole, and then extracting from its pole the LSP resonance frequency. However, it was shown in the numerical study of Venermo & Sihvola [65] that the polarizability of a cylinder closely matches the closed-form expression for

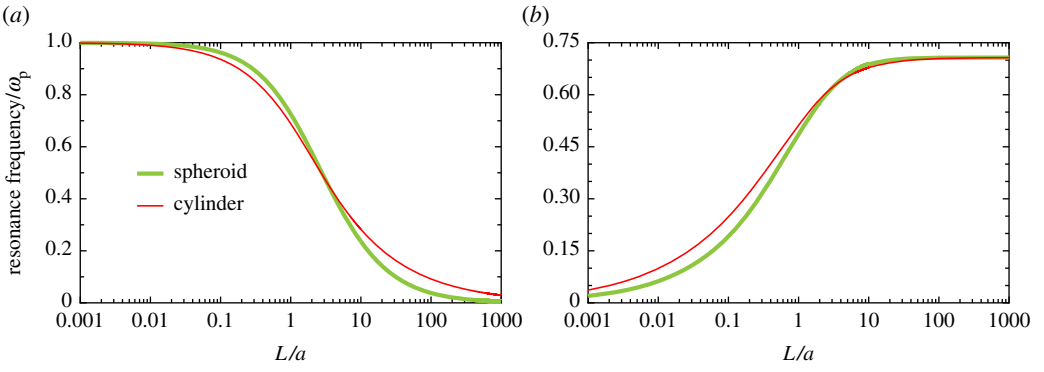

Figure 5. Resonance frequencies of the LSPs in a spheroidal (thick green lines) and cylindrical (thin red lines) nanoparticle, in units of the plasma frequency ω_p, as a function of the aspect ratio L/a. (*a*) Longitudinal mode. (*b*) Transverse mode. The analytical expressions for the cylinder are given by (2.14) and (2.20), and for the spheroid the closed-form expressions can be found, for example, in [11]. (Online version in colour.)

the polarizability of a spheroid (i.e. an ellipsoid of revolution) with the same length-to-diameter ratio.

In this appendix, we provide a comparison between two sets of analytical results for the LSP resonance frequency in the quasi-static regime: firstly, our closed-form expressions for cylinders as derived in §2, and secondly the well-known expressions for a spheroid that can be found, for example, in [11]. We consider the spheroid to be described by the semi-axes $L/2$ and a, so that it closely resembles the cylinder considered in the main text (of length L and diameter $2a$). By modulating the aspect ratio L/a governing the spheroid geometry, we can describe oblate spheroids ($L < 2a$), spheres ($L = 2a$), and prolate spheroids ($L > 2a$). Crucially, spheroids share their limiting forms with cylinders: in the limit $L \ll a$ they both reduce to disks, and in the opposing limit $L \gg a$ they both become wires.

In figure 5, we plot the LSP resonance frequencies as a function of the aspect ratio L/a, for both the longitudinal and transverse polarizations. The standard textbook expressions for a spheroid are given in [11, pp. 146, 345], and the cylindrical results of this work are given by (2.14) and (2.20). As was found in the numerical comparison of [65], there is a very good agreement between the spheroid (thick green lines) and the cylinder (thin red lines) as they evolve geometrically. The correspondence is perfect in the extreme disk and wire limits.

The small discrepancies in resonance frequency between the two geometries can be analysed by considering the asymptotics of the spheroid. In the longitudinal polarization, the resonance frequency (in units of the plasma frequency ω_p) approaches $1 - \pi L/8a$ in the disk limit ($L \ll a$), and $(2a/L)[\ln(L/a) - 1]^{1/2}$ in the wire limit. Therefore, as shown in figure 5*a*, the agreement is excellent in the disk limit, since both the spheroid and cylinder frequencies scale linearly with L/a (cf. (2.15)). In the wire limit ($L \gg a$), while the L/a scaling is inverse linear for the spheroid, it is inverse square root for the cylinder (cf. (2.16)). For the transverse polarization, the spheroid asymptotics is $(\pi L/8a)^{1/2}$ in the disk limit, displaying the same square root scaling as the cylinder (cf. (2.21)). In the wire limit, the spheroid behaviour is described by $\{1 - 2(a/L)^2[\ln(L/a) - 1]\}/\sqrt{2}$, an inverse square behaviour which differs from the inverse linear scaling for the cylinder (cf. (2.22)), but does not lead to a noticeable deviation on the scale of figure 5*b*.

We conclude that, as shown numerically in [65], the plasmonic behaviour of spheroids and cylinders is indeed very similar. Our closed-form expressions for the cylinder provide insight into the small differences between the two geometries, most prominently in the wire limit asymptotics, and challenge the long-held notion that only spheres and spheroids may be characterized analytically.

Appendix B. Schrödinger equation with a cylindrical step potential

In this appendix, we provide details about the bound-state solutions to the Schrödinger equation (3.7), which enable us to evaluate semiclassically the average number of spill-out electrons (3.4), in both the longitudinal and transverse directions.

Separating the variables as in (3.8), the transverse wave functions $F_{nm}(r,\theta)$ are subject to the following Schrödinger equation:

$$\left\{\frac{\partial^2}{\partial r^2}+\frac{1}{r}\frac{\partial}{\partial r}+\frac{1}{r^2}\frac{\partial^2}{\partial\theta^2}+\left[k_r^2-\frac{2m_\mathrm{e}}{\hbar^2}V_r(r)\right]\right\}F_{nm}(r,\theta)=0. \tag{B 1}$$

With the ansatz $F_{nm}(r,\theta)=R_{nm}(r)\,\mathrm{e}^{\mathrm{i}m\theta}/(2\pi)^{1/2}$, where the quantum number $m\in\mathbb{Z}$, and with the notation $\kappa_r=(k_0^2-k_r^2)^{1/2}$, where $k_0=(2m_\mathrm{e}V_0/\hbar^2)^{1/2}$, one finds the following bound state solutions:

$$R_{nm}(r)=C_{nm}\begin{cases}J_m(k_r r), & r\le a,\\ \dfrac{J_m(k_r a)}{K_m(\kappa_r a)}K_m(\kappa_r r), & r>a,\end{cases} \tag{B 2}$$

where $J_m(x)$ and $K_m(x)$ are the Bessel functions of the first and second kinds, respectively. The normalization constant in (B 2) is given by

$$C_{nm}=\frac{\sqrt{2}}{a}\left\{\left[\frac{J_m(k_r a)}{K_m(\kappa_r a)}\right]^2 K_{m+1}(\kappa_r a)K_{m-1}(\kappa_r a)-J_{m+1}(k_r a)J_{m-1}(k_r a)\right\}^{-1/2}, \tag{B 3}$$

while the transverse motion is subject to energy quantization via the transcendental equation $k_r J_{m+1}(k_r a)/J_m(k_r a)=\kappa_r K_{m+1}(\kappa_r a)/K_m(\kappa_r a)$, whose solutions are labelled with the quantum number n.

The longitudinal wave functions $Z_{\tilde{n}}(z)$ entering (3.8) obey

$$\frac{\mathrm{d}^2}{\mathrm{d}z^2}Z_{\tilde{n}}(z)+\left[k_z^2-\frac{2m_\mathrm{e}}{\hbar^2}V_z(z)\right]Z_{\tilde{n}}(z)=0, \tag{B 4}$$

which is equivalent to the textbook quantum mechanics exercise of a one-dimensional particle in a square box [74]. The solutions of (B 4) have either a symmetric (s) or an antisymmetric (a) parity, which we specify as $Z_{\tilde{n}}(z)=Z_{\tilde{n},\mathrm{p}}(z)$, where the index $\mathrm{p}=(\mathrm{s},\mathrm{a})$. The even bound state solutions are given by

$$Z_{\tilde{n},\mathrm{s}}(z)=\sqrt{\frac{\kappa_z}{1+\kappa_z L/2}}\begin{cases}\cos\left(\dfrac{k_z L}{2}\right)\mathrm{e}^{\kappa_z(L/2+z)}, & z\le-\dfrac{L}{2},\\ \cos(k_z z), & |z|<\dfrac{L}{2},\\ \cos\left(\dfrac{k_z L}{2}\right)\mathrm{e}^{\kappa_z(L/2-z)}, & z\ge\dfrac{L}{2},\end{cases} \tag{B 5a}$$

where $\kappa_z=(k_0^2-k_z^2)^{1/2}>0$. Similarly, the odd solutions read

$$Z_{\tilde{n},\mathrm{a}}(z)=\sqrt{\frac{\kappa_z}{1+\kappa_z L/2}}\begin{cases}-\sin\left(\dfrac{k_z L}{2}\right)\mathrm{e}^{\kappa_z(L/2+z)}, & z\le-\dfrac{L}{2},\\ \sin(k_z z), & |z|<\dfrac{L}{2},\\ \sin\left(\dfrac{k_z L}{2}\right)\mathrm{e}^{\kappa_z(L/2-z)}, & z\ge\dfrac{L}{2}.\end{cases} \tag{B 5b}$$

Both sets of eigenfunctions (B 5*a*) and (B 5*b*) are associated with an individual transcendental equation describing the quantization of energy due to the longitudinal confinement, explicitly $\tan(k_z L/2)=\kappa_z/k_z$ (s modes) and $\tan(k_z L/2)=-k_z/\kappa_z$ (a modes). The solutions of these equations are labelled with the third quantum number of the problem, $\tilde{n}$.

Now that the full Schrödinger equation (3.7) is solved, we proceed with the evaluation of the integrals entering (3.4), namely

$$\mathcal{R}_{nm}^{\mathrm{in}} = \int_0^a \mathrm{d}r\, r\, |R_{nm}(r)|^2, \quad \mathcal{R}_{nm}^{\mathrm{out}} = \int_a^\infty \mathrm{d}r\, r |R_{nm}(r)|^2 \tag{B 6}$$

and

$$\mathcal{Z}_{\tilde{n},\mathrm{p}}^{\mathrm{in}} = \int_{-L/2}^{+L/2} \mathrm{d}z\, |Z_{\tilde{n},\mathrm{p}}(z)|^2, \quad \mathcal{Z}_{\tilde{n},\mathrm{p}}^{\mathrm{out}} = \left(\int_{-\infty}^{-L/2} + \int_{+L/2}^{+\infty}\right) \mathrm{d}z\, |Z_{\tilde{n},\mathrm{p}}(z)|^2, \tag{B 7}$$

which describe the probability of finding the electrons inside or outside the cylindrical NP, in either the transverse or longitudinal directions. With (B 2), we obtain for the transverse integrals (B 6) the results

$$\mathcal{R}_{nm}^{\mathrm{in}} = \frac{J_{m+1}(k_r a)J_{m-1}(k_r a) - J_m^2(k_r a)}{J_{m+1}(k_r a)J_{m-1}(k_r a) - J_m^2(k_r a)K_{m+1}(\kappa_r a)K_{m-1}(\kappa_r a)/K_m^2(\kappa_r a)} \tag{B 8a}$$

and

$$\mathcal{R}_{nm}^{\mathrm{out}} = \frac{K_{m+1}(\kappa_r a)K_{m-1}(\kappa_r a) - K_m^2(\kappa_r a)}{K_{m+1}(\kappa_r a)K_{m-1}(\kappa_r a) - K_m^2(\kappa_r a)J_{m+1}(k_r a)J_{m-1}(k_r a)/J_m^2(k_r a)}. \tag{B 8b}$$

Similarly, using (B 5), we find for the longitudinal integrals (B 7)

$$\mathcal{Z}_{\tilde{n},\mathrm{p}}^{\mathrm{in}} = \frac{1}{1+\kappa_z L/2}\left(\frac{\kappa_z L}{2} + \frac{\kappa_z^2}{k_0^2}\right) \quad \text{and} \quad \mathcal{Z}_{\tilde{n},\mathrm{p}}^{\mathrm{out}} = \frac{k_z^2/k_0^2}{1+\kappa_z L/2}. \tag{B 9}$$

In the high-energy semiclassical limit ($k_0 a \gg 1, k_0 L \gg 1$), which is well suited for the problem at hand [69], we find that the expressions (B 8) and (B 9) are well approximated by

$$\mathcal{R}_{nm}^{\mathrm{in}} \simeq 1, \quad \mathcal{R}_{nm}^{\mathrm{out}} \simeq \frac{1}{2}\frac{1}{\kappa_r a}, \quad \mathcal{Z}_{\tilde{n},\mathrm{p}}^{\mathrm{in}} \simeq 1 \quad \text{and} \quad \mathcal{Z}_{\tilde{n},\mathrm{p}}^{\mathrm{out}} \simeq \frac{2}{\kappa_z L}\frac{k_z^2}{k_0^2}, \tag{B 10}$$

which then lead to (3.9).[5]

Appendix C. Toy model: two coupled oscillating dipoles

In this appendix, we demonstrate that the results (4.8) and (4.13) for the resonance frequencies of the coupled modes in a dimer of cylindrical NPs in the limit of large interparticle separation distance (i.e. $d/a \gg 1$ and $d/L \gg 1$) can be recovered from a toy model of two coupled anisotropic oscillating dipolar moments.

Let us consider two ideal electric dipoles $\mathbf{p}_i = -N_\mathrm{e} e\, \mathbf{r}_i$ $(i = 1, 2)$, with $\mathbf{r}_i$ the associated displacement of the electronic cloud with charge $-N_\mathrm{e} e$ and mass $N_\mathrm{e} m_\mathrm{e}$. The dimer (with interparticle distance d) is aligned along the z-direction and each dipole oscillates at the frequency $\omega_{0,\parallel}^{\mathrm{dip}}$ in the longitudinal (z) direction and $\omega_{0,\perp}^{\mathrm{dip}}$ in the transverse (x, y) directions. The Lagrangian for the system described above reads

$$\mathcal{L} = \frac{N_\mathrm{e} m_\mathrm{e}}{2}\sum_{i=1}^{2}\left[\dot{\mathbf{r}}_i^2 - \omega_{0,\perp}^{\mathrm{dip}\,2}\left(x_i^2 + y_i^2\right) - \omega_{0,\parallel}^{\mathrm{dip}\,2} z_i^2\right] - \frac{N_\mathrm{e}^2 e^2}{d^3}\left[\mathbf{r}_1\cdot\mathbf{r}_2 - 3\left(\mathbf{r}_1\cdot\hat{z}\right)\left(\mathbf{r}_2\cdot\hat{z}\right)\right]. \tag{C 1}$$

Using that $N_\mathrm{e} e^2/m_\mathrm{e} = \omega_\mathrm{p}^2 V/4\pi$, with V the volume of the electronic cloud, the Euler–Lagrange equations of motion for the toy model (C 1) lead to the coupled mode resonance frequencies

$$\omega_{\tau,\parallel}^{\mathrm{dip}} = \sqrt{\omega_{0,\parallel}^{\mathrm{dip}\,2} + 2\tau\omega_\mathrm{p}^2\frac{V}{4\pi d^3}}, \quad \omega_{\tau,\perp}^{\mathrm{dip}} = \sqrt{\omega_{0,\perp}^{\mathrm{dip}\,2} + \tau\omega_\mathrm{p}^2\frac{V}{4\pi d^3}}, \quad \tau = \pm. \tag{C 2}$$

[5]In this semiclassical limit, the leading order expressions (B 10) do not satisfy unitarity, which requires the inclusion of high-order terms. However, since the absent terms are of negligible importance for the range of parameters we consider in this work we may omit them. Notably, this semiclassical limit has been shown to be an excellent approximation for a spherical NP [69] and it has the significant advantage of providing additional physical insight.

With $V = \pi a^2 L$ the volume of the cylinder considered in the main text, the expressions above correspond to (4.8) and (4.13) with Ω given by (4.10) in the limit of $d/a \gg 1$ and $d/L \gg 1$.

References

1. Kreibig U, Vollmer M. 1995 *Optical properties of metal clusters*. Berlin, Germany: Springer.
2. Maier SA. 2007 *Plasmonics: fundamentals and applications*. New York, NY: Springer.
3. Ozbay E. 2006 Plasmonics: merging photonics and electronics at nanoscale dimensions. *Science* **311**, 189–193. (doi:10.1126/science.1114849)
4. Barnes WL, Dereux A, Ebbesen TW. 2003 Surface plasmon subwavelength optics. *Nature* **424**, 824–830. (doi:10.1038/nature01937)
5. Gramotnev DK, Bozhevolnyi SI. 2010 Plasmonics beyond the diffraction limit. *Nat. Photon.* **4**, 83–91. (doi:10.1038/nphoton.2009.282)
6. Stockman MI. 2011 Nanoplasmonics: past, present, and glimpse into future. *Opt. Express* **19**, 22029. (doi:10.1364/OE.19.022029)
7. Tame MS, McEnery KR, Ozdemir SK, Lee J, Maier SA, Kim MS. 2013 Quantum plasmonics. *Nat. Phys.* **9**, 329–340. (doi:10.1038/nphys2615)
8. García de Abajo FJ. 2010 Optical excitations in electron microscopy. *Rev. Mod. Phys.* **82**, 209–275. (doi:10.1103/RevModPhys.82.209)
9. Kerker U. 1969 *The scattering of light, and other electromagnetic radiation*. New York, NY: Academic Press.
10. van de Hulst HC. 1981 *Light scattering by small particles*. New York, NY: Dover.
11. Bohren CF, Huffman DR. 1983 *Absorption and scattering of light by small particles*. New York, NY: Wiley.
12. Mishchenko MI, Hovenier JW, Travis LD. 2000 *Light scattering by nonspherical particles: theory, measurements, and applications*. San Diego, CA: Academic Press.
13. Mishchenko MI, Travis LD, Lacis AA. 2002 *Scattering, absorption, and emission of light by small particles*. Cambridge, UK: Cambridge University Press.
14. Mayergoyz ID. 2013 *Plasmon resonances in nanoparticles*. Singapore: World Scientific.
15. Schmidt FP, Ditlbacher H, Hohenester U, Hohenau A, Hofer F, Krenn JR. 2012 Dark plasmonic breathing modes in silver nanodisks. *Nano Lett.* **12**, 5780–5783. (doi:10.1021/nl3030938)
16. Juvé V, Fernanda Cardinal M, Lombardi A, Crut A, Maioli P, Pérez-Juste J, Liz-Marzán LM, Del Fatti N, Vallée F. 2013 Size-dependent surface plasmon resonance broadening in nonspherical nanoparticles: single gold nanorods. *Nano Lett.* **13**, 2234–2240. (doi:10.1021/nl400777y)
17. Schmidt FP, Ditlbacher H, Hofer F, Krenn JR, Hohenester U. 2014 Morphing a plasmonic nanodisk into a nanotriangle. *Nano Lett.* **14**, 4810–4815. (doi:10.1021/nl502027r)
18. Krug MK, Reisecker M, Hohenau A, Ditlbacher H, Trugler A, Hohenester U, Krenn JR. 2014 Probing plasmonic breathing modes optically. *Appl. Phys. Lett.* **105**, 171103. (doi:10.1063/1.4900615)
19. Wang H, Wang X, Yan C, Zhao H, Zhang J, Santschi C, Martin OJF. 2017 Full color generation using silver tandem nanodisks. *ACS Nano* **11**, 4419–4427. (doi:10.1021/acsnano.6b08465)
20. Movsesyan A, Baudrion AL, Adam PM. 2018 Revealing the hidden plasmonic modes of a gold nanocylinder. *J. Phys. Chem. C* **122**, 23 651–23 658. (doi:10.1021/acs.jpcc.8b05705)
21. Schmidt FP, Losquin A, Hofer F, Hohenau A, Krenn JR, Kociak M. 2018 How dark are radial breathing modes in plasmonic nanodisks? *ACS Photonics* **5**, 861–866. (doi:10.1021/acsphotonics.7b01060)
22. Bertsch GF, Broglia RA. 1994 *Oscillations in finite quantum systems*. Cambridge, UK: Cambridge University Press.
23. Luk'yanchuk BS, Ternovsky V. 2006 Light scattering by a thin wire with a surface-plasmon resonance: bifurcations of the Poynting vector field. *Phys. Rev. B* **73**, 235432. (doi:10.1103/PhysRevB.73.235432)
24. Abrashuly A, Valagiannopoulos C. 2019 Limits for absorption and scattering by core-shell nanowires in the visible spectrum. *Phys. Rev. Appl.* **11**, 014051. (doi:10.1103/PhysRevApplied.11.014051)
25. Gangaraj SAH, Valagiannopoulos C, Monticone F. 2020 Topological scattering resonances at ultralow frequencies. *Phys. Rev. Res.* **2**, 023180. (doi:10.1103/PhysRevResearch.2.023180)
26. Schroter U, Dereux A. 2001 Surface plasmon polaritons on metal cylinders with dielectric core. *Phys. Rev. B* **64**, 125420. (doi:10.1103/PhysRevB.64.125420)

27. Mayergoyz ID, Fredkin DR, Zhang Z. 2005 Electrostatic (plasmon) resonances in nanoparticles. *Phys. Rev. B* **72**, 155412. (doi:10.1103/PhysRevB.72.155412)
28. Sburlan SE, Blanco LA, Nieto-Vesperinas M. 2006 Plasmon excitation in sets of nanoscale cylinders and spheres. *Phys. Rev. B* **73**, 035403. (doi:10.1103/PhysRevB.73.035403)
29. Amendola V, Bakr OM, Stellacci F. 2010 A study of the surface plasmon resonance of silver nanoparticles by the discrete dipole approximation method: effect of shape, size, structure, and assembly. *Plasmonics* **5**, 85–97. (doi:10.1007/s11468-009-9120-4)
30. Tserkezis C, Stefanou N. 2012 Calculation of waveguide modes in linear chains of metallic nanorods. *J. Opt. Soc. Am. B* **29**, 827. (doi:10.1364/JOSAB.29.000827)
31. Napoles-Duarte JM, Chavez-Rojo MA, Fuentes-Montero ME, Rodriguez-Valdez LM, Garcia-Llamas R, Gaspar-Armenta JA. 2015 Surface plasmon resonances in Drude metal cylinders: radius dependence and quality factor. *J. Opt.* **17**, 065003. (doi:10.1088/2040-8978/17/6/065003)
32. Brack M. 1993 The physics of simple metal clusters: self-consistent jellium model and semiclassical approaches. *Rev. Mod. Phys.* **65**, 677–732. (doi:10.1103/RevModPhys.65.677)
33. Skjolstrup EJH, Sondergaard T, Pedersen TG. 2018 Quantum spill out in few-nanometer metal gaps: effect on gap plasmons and reflectance from ultrasharp groove arrays. *Phys. Rev. B* **97**, 115429. (doi:10.1103/PhysRevB.97.115429)
34. Prodan E, Radloff C, Halas NJ, Nordlander P. 2003 A hybridization model for the plasmon response of complex nanostructures. *Science* **302**, 419–164. (doi:10.1016/j.cplett.2010.01.062)
35. Jain PK, El-Sayed MA. 2010 Plasmonic coupling in noble metal nanostructures. *Chem. Phys. Lett.* **487**, 153–164. (doi:10.1016/j.cplett.2010.01.062)
36. Sahoo PK, Vogelsang K, Schift H, Solak HH. 2009 Surface plasmon resonance in near-field coupled gold cylinder arrays fabricated by EUV-interference lithography and hot embossing. *Appl. Surf. Sci.* **256**, 431–434. (doi:10.1016/j.apsusc.2009.06.079)
37. Guillot N, Shen H, Fremaux B, Peron O, Rinnert E, Toury T, Lamy de la Chapelle M. 2010 Surface enhanced Raman scattering optimization of gold nanocylinder arrays: influence of the localized surface plasmon resonance and excitation wavelength. *Appl. Phys. Lett.* **97**, 023113. (doi:10.1063/1.3462068)
38. Zoric I, Zach M, Kasemo B, Langhammer C. 2011 Gold, platinum, and aluminum nanodisk plasmons: material independence, subradiance, and damping mechanisms. *ACS Nano* **5**, 2535–2546. (doi:10.1021/nn102166t)
39. Gillibert R, Colas F, Yasukuni R, Picardi G, Lamy de la Chapelle M. 2017 Plasmonic properties of aluminum nanocylinders in the visible range. *J. Phys. Chem. C* **121**, 2402–2409. (doi:10.1021/acs.jpcc.6b11779)
40. Kawachiya Y, Murai S, Saito M, Sakamoto H, Fujita K, Tanaka K. 2018 Collective plasmonic modes excited in Al nanocylinder arrays in the UV spectral region. *Opt. Express* **26**, 5970–5982. (doi:10.1364/OE.26.005970)
41. Maier SA, Kik PG, Atwater HA, Meltzer S, Harel E, Koel BE, Requicha AAG. 2003 Local detection of electromagnetic energy transport below the diffraction limit in metal nanoparticle plasmon waveguides. *Nat. Mater.* **2**, 229–232. (doi:10.1038/nmat852)
42. Brandstetter-Kunc A, Weick G, Downing CA, Weinmann D, Jalabert RA. 2016 Nonradiative limitations to plasmon propagation in chains of metallic nanoparticles. *Phys. Rev. B* **94**, 205432. (doi:10.1103/PhysRevB.94.205432)
43. Cole JR, Halas NJ. 2006 Optimized plasmonic nanoparticle distributions for solar spectrum harvesting. *Appl. Phys. Lett.* **89**, 153120. (doi:10.1063/1.2360918)
44. Aubry A, Lei DY, Fernandez-Dominguez AI, Sonnefraud Y, Maier SA, Pendry JB. 2010 Plasmonic light-harvesting devices over the whole visible spectrum. *Nano Lett.* **10**, 2574–2579. (doi:10.1021/nl101235d)
45. Poddubny A, Miroshnichenko A, Slobozhanyuk A, Kivshar Y. 2014 Topological Majorana states in zigzag chains of plasmonic nanoparticles. *ACS Photonics* **1**, 101–105. (doi:10.1021/ph4000949)
46. Downing CA, Weick G. 2017 Topological collective plasmons in bipartite chains of metallic nanoparticles. *Phys. Rev. B* **95**, 125426. (doi:10.1103/PhysRevB.95.125426)
47. Downing CA, Weick G. 2018 Topological plasmons in dimerized chains of nanoparticles: robustness against long-range quasistatic interactions and retardation effects. *Eur. Phys. J. B* **91**, 253. (doi:10.1140/epjb/e2018-90199-0)

48. Pocock SR, Xiao X, Huidobro PA, Giannini V. 2018 Topological plasmonic chain with retardation and radiative effects. *ACS Photonics* **5**, 2271–2279. (doi:10.1021/acsphotonics.8b00117)
49. Nordlander P, Oubre C, Prodan E, Li K, Stockman MI. 2004 Plasmon hybridization in nanoparticle dimers. *Nano Lett.* **4**, 899–903. (doi:10.1021/nl049681c)
50. Reinhard BM, Siu M, Agarwal H, Alivisatos AP, Liphardt J. 2005 Calibration of dynamic molecular rulers based on plasmon coupling between gold nanoparticles. *Nano Lett.* **5**, 2246–2252. (doi:10.1021/nl051592s)
51. Jain PK, Huang W, El-Sayed MA. 2007 On the universal scaling behavior of the distance decay of plasmon coupling in metal nanoparticle pairs: a plasmon ruler equation. *Nano Lett.* **7**, 2080–2088. (doi:10.1021/nl071008a)
52. Brandstetter-Kunc A, Weick G, Weinmann D, Jalabert RA. 2015 Decay of dark and bright plasmonic modes in a metallic nanoparticle dimer. *Phys. Rev. B* **91**, 035431. (doi:10.1103/PhysRevB.91.03543). Erratum: *Phys. Rev. B* **92**, 199906. (doi:10.1103/PhysRevB.92.199906)
53. Chu MW, Myroshnychenko V, Chen CH, Deng JP, Mou CY, Garcia de Abajo FJ. 2009 Probing bright and dark surface-plasmon modes in individual and coupled noble metal nanoparticles using an electron beam. *Nano Lett.* **9**, 399–404. (doi:10.1021/nl803270x)
54. Koh AL, Bao K, Khan I, Smith WE, Kothleitner G, Nordlander P, Maier SA, McComb DW. 2009 Electron energy loss spectroscopy (EELS) of surface plasmons in single silver nanoparticles and dimers: influence of beam damage and mapping of dark modes. *ACS Nano* **3**, 3015–3022. (doi:10.1021/nn900922z)
55. Barrow SJ, Rossouw D, Funston AM, Botton GA, Mulvaney P. 2014 Mapping bright and dark modes in gold nanoparticle chains using electron energy loss spectroscopy. *Nano Lett.* **14**, 3799–3808. (doi:10.1021/nl5009053)
56. Kottmann JP, Martin OJF. 2001 Plasmon resonant coupling in metallic nanowires. *Opt. Express* **8**, 665–663. (doi:10.1364/OE.8.000655)
57. Hoflich K, Gosele U, Christiansen S. 2009 Near-field investigations of nanoshell cylinder dimers. *J. Chem. Phys.* **131**, 164704. (doi:10.1063/1.3231870)
58. Vorobev PE. 2010 Electric field enhancement between two parallel cylinders due to plasmonic resonance. *J. Exp. Theor. Phys.* **110**, 193–198. (doi:10.1134/S1063776110020020)
59. Babicheva VE, Vergeles SS, Vorobev PE, Burger S. 2012 Localized surface plasmon modes in a system of two interacting metallic cylinders. *J. Opt. Soc. Am. B* **29**, 1263–1269. (doi:10.1364/JOSAB.29.001263)
60. Toscano G, Raza S, Jauho AP, Mortensen NA, Wubs M. 2012 Modified field enhancement and extinction by plasmonic nanowire dimers due to nonlocal response. *Opt. Express* **20**, 4176–4188. (doi:10.1364/OE.20.004176)
61. Schnitzer O, Giannini V, Maier SA, Craster RV. 2016 Surface plasmon resonances of arbitrarily shaped nanometallic structures in the small-screening-length limit. *Proc. R. Soc. A* **472**, 20160258. (doi:10.1098/rspa.2016.0258)
62. Bereza AS, Frumin LL, Nemykin AV, Perminov SV, Shapiro DA. 2019 Perturbation series for the scattering of electromagnetic waves by parallel cylinders. *EPL* **127**, 20002. (doi:10.1209/0295-5075/127/20002)
63. Yin Y, Hervieux PA, Jalabert RA, Manfredi G, Maurat E, Weinmann D. 2009 Spin-dependent dipole excitation in alkali-metal nanoparticles. *Phys. Rev. B* **80**, 115416. (doi:10.1103/PhysRevB.80.115416)
64. Jackson JD. 1998 *Classical electrodynamics*. New York, NY: Wiley.
65. Venermo J, Sihvola A. 2005 Dielectric polarizability of circular cylinder. *J. Electrostat.* **63**, 101–117. (doi:10.1016/j.elstat.2004.09.001)
66. Slachmuylders AF, Partoens B, Magnus W, Peeters FM. 2006 Dielectric mismatch effect on the exciton states in cylindrical nanowires. *Phys. Rev. B* **74**, 235321. (doi:10.1103/PhysRevB.74.235321)
67. Weick G, Molina RA, Weinmann D, Jalabert RA. 2005 Lifetime of the first and second collective excitations in metallic nanoparticles. *Phys. Rev. B* **72**, 115410. (doi:10.1103/PhysRevB.72.115410)
68. Brack M, Bhaduri RK. 1997 *Semiclassical physics*. Reading, MA: Addison-Wesley.
69. Weick G, Ingold GL, Jalabert RA, Weinmann D. 2006 Surface plasmon in metallic nanoparticles: renormalization effects due to electron-hole excitations. *Phys. Rev. B* **74**, 165421. (doi:10.1103/PhysRevB.74.165421)

70. Park SY, Stroud D. 2004 Surface-plasmon dispersion relations in chains of metallic nanoparticles: an exact quasistatic calculation. *Phys. Rev. B* **69**, 125418. (doi:10.1103/PhysRevB.69.125418)
71. Downing CA, Mariani E, Weick G. 2017 Radiative frequency shifts in nanoplasmonic dimers. *Phys. Rev. B* **96**, 155421. (doi:10.1103/PhysRevB.96.155421)
72. Weber WH, Ford GW. 2004 Propagation of optical excitations by dipolar interactions in metal nanoparticle chains. *Phys. Rev. B* **70**, 125429. (doi:10.1103/PhysRevB.70.125429)
73. Downing CA, Mariani E, Weick G. 2018 Retardation effects on the dispersion and propagation of plasmons in metallic nanoparticle chains. *J. Phys.: Condens. Matter* **30**, 025301. (doi:10.1088/1361-648X/aa9d59)
74. Cohen-Tannoudji C, Diu B, Laloë F. 2019 *Quantum mechanics. Volume I: basic concepts, tools, and applications*. Weinheim, Germany: Wiley-VCH.